LAWRENCE
LIVERMORE
NATIONAL
LABORATORY

UCRL-JRNL-215836

Assessment of a Single-Shot Pixelated Phase-Shifting Interferometer Utilizing a Liquid Crystal Spatial Light Modulator

K. L. Baker, E. A. Stappaerts

October 3, 2005

Optics Letters

Disclaimer

Assessment of a Single-Shot Pixelated Phase-Shifting Interferometer Utilizing a Liquid Crystal Spatial Light Modulator

K.L. Baker, et al.

Lawrence Livermore National Laboratory, Livermore, CA, USA

Abstract

This article introduces a novel phase shifting pixelated interferometer based on a liquid crystal spatial light modulator and simulates the expected performance. The phase shifted frames are captured simultaneously which reduces the problems arising from vibrations and air turbulence. The liquid crystal spatial light modulator is very flexible and can be configured to provide a large number of phase shift levels and geometries to reduce the measurement error.

OCIS codes: 120.3180 Interferometry, 120.3930 Metrological instrumentation, 120.5050 Phase measurement

Phase-shifting interferometry is a highly accurate and widely used technique for measuring the wave-front phase between a test and reference optical path. Phase shifting interferometers can be placed into two categories: instruments that collect the interferograms simultaneously, spatial phase shifting interferometers, and instruments collect the interferograms sequentially as the phase in the reference beam is shifted, temporal phase shifting interferometers.[1] In temporal phase shifting interferometers, typically a single detector is used to record a single phase-shifted interferogram each time the reference beam path length is varied to obtain a number of different phase-shifted interferograms. In spatial phase-shifting interferometers, multiple interferograms are recorded simultaneously with a relative phase shift on the reference beams between the different interferograms. The spatially shifted interferograms can be recorded on separate detectors or multiplexed on a single detector. Recently a pixelated phase-shifting interferometer was introduced in which four separate phase-shifted interferograms were spatially multiplexed into a single interferogram.[2] This instrument utilizes micro-polarizers in conjunction with circularly polarized light to obtain multiplexed phase shifting on a single detector array. There have also been several implementations of phase shifting interferometers which utilize liquid-crystal spatial light modulators to perform temporal phase shifting[3,4,5] and spatial phase shifting[6,7]. In this article we present an interferometer design using two linearly polarized beams in conjunction with a liquid-crystal spatial light modulator to obtain a pixelated phase shifting interferometer on a single camera with an arbitrary number of phase shifts.

A pixelated phase shifting interferometer design utilizing a liquid-crystal spatial light modulator(LC-SLM) is shown in Figure 1. The LC-SLM is placed such that both

the reference and probe beams are reflected from the surface. Therefore the only non-common path phase introduced by the LC-SLM is the pixelated index of refraction changes induced by the applied voltage and not the intrinsic aberrations of the unpowered LC-SLM. In the design shown in Fig. 1a, a laser is incident on a non-polarizing beam splitter before reflection from the LC-SLM. The laser is polarized at 45 degrees relative to the axis of the spatial light modulator. The LC-SLM is used to introduce a pixelated discreet phase change between the two polarizations. The light is then reflected back to the non-polarizing beamsplitter before entering the Twyman-Green configuration. A polarizing beamsplitter is used to separate the two orthogonally polarized beams, passing the probe beam through the test object before being recombined with the reference beam using the same polarizing beamsplitter. The LC-SLM should be at a conjugate image plane of the object being measured, which should in turn be at a conjugate image plane of the wave-front sensing camera. There should also be a 1:1 correspondence between the LC-SLM pixels and the pixels on the wave-front sensing camera. A self-referencing point diffraction version of the pixilated phase shifting interferometer is shown in Fig. 1b. In this case a polarizing pinhole mask[2] is used to generate the reference and probe beams.

A number of different phase maps can be written to the LC-SLM and they can be easily changed as shown in Figure 2. In this figure three different geometries for three four and five separate phase levels are displayed as shown in a, b and c respectively. The phase levels can be easily changed as well. For instance in the case of the three channel interferometer, the phases could be 0, 120 and 240 degrees rather than 45, 135 and 225 as shown. Because the spatial light modulator can trivially change its phase masks, this interferometer allows the tradeoff between measurement error and spatial resolution.

Lower measurement errors can be obtained at low spatial frequencies by using a large number of phase steps but higher spatial resolution can be obtained with a smaller number of phase steps at the expense of higher measurement noise.

The overall accuracy of the interferometer will likely depend on how well the spatial light modulator is calibrated. The performance of the interferometer as a function of random errors in the calibration of the phase steps applied to the liquid-crystal spatial light modulator was simulated by applying random errors of a specified amplitude to the four channels of the interferometer. The errors in the phase steps are uniformly distributed between $\pm$ 0.5 of the phase error given in the abscissa of Fig. 3. A sinusoidal phase profile was used as the phase profile to be reconstructed. Intensity profiles were made from a uniform amplitude and the given sinusoidal phase profile with random phase perturbations added to the reference phase shifts. The phase profile was then determined using the standard reconstruction formula for a four-bin interferometer, $\mathrm{Tan}(\phi)=(I_4-I_2)/(I_1-I_3)$ with phase steps in the references of the four channels of $0(I_1)$, $\pi/2(I_2)$, $\pi(I_3)$ and $3\pi/2(I_4)$, respectively.[1] Figure 3 shows the results of the variance of the reconstructed phase as a function of random error applied to the LC-SLM. The simulated variance is represented by the solid black circles and an analytic derivation, as detailed below, of the error is represented by the solid gray line.

An analytic representation to the phase can also be derived. In the case of a four-bin interferometer, random perturbations of α, β, γ and δ are added to the phase steps above. The effective change in the measured phase, ζ, can then be found by taking the standard formula for the reconstructed phase, $\mathrm{Tan}(\phi+\zeta)=(I_4-I_2)/(I_1-I_3)$, from the four channels and making the assumption that the random phase perturbations added(α, β, γ

and δ) to the channels(I_1, I_2, I_3 and I_4) are small. Keeping terms of the order of the random phase perturbation, the effective change in the measured phase is found to be ζ=(δ+β)/2. The phase perturbations δ and β are assumed to be random such that the magnitude of the change in the measured phase would be expected to be ζ~δ/SQRT(2). Assuming that the errors in the phase measurement are uniformly distributed spatially across the measurement, then the variance, σ^2, may be expressed by $\sigma^2 \approx \frac{1}{\zeta}\int_0^{\zeta}\left(\phi - \frac{\zeta}{2}\right)^2 \mathrm{d}\phi = \frac{\zeta^2}{12}$.[8] The variance as a result of random phase perturbations in the phase steps would then be given by $\sigma^2 \sim \delta^2/24$, where δ represents the magnitude of the random phase perturbations added to each of the phase steps. The analytic variance of $\sigma^2 = \delta^2/24$ is drawn in Fig. 3 as the light gray line and agrees very well with the simulations.

In the case of a pixelated spatial phase shifting interferometer, a macro-pixel consisting of some number of pixels with different phase delays is used to reconstruct the phase and the spatial resolution of the interferometer is reduced from that achievable by an individual pixel. For a four-bin phase mask, the phase can be reconstructed at the corners where all of the four separate phase pixels comprising a macro-pixel touch each other. This phase reconstructed in this manner has a pitch equivalent to a single pixel within the macro-pixel, twice that of the macro-pixel for a four-bin interferometer. This will be referred to as algorithm 1(alg. 1) or the nearest neighbor alg. below. To obtain the phase in the center of the pixels, an averaging of the phase in the four corners, which involves phase information from the closest nine pixels including the reconstructed pixel,

must be performed as quantified by Eq. 1, alg. 2, or the use of a nine-pixel region[2] can be used to reconstruct the phase as expressed by Eq. 2, alg. 3.

$$\text{Phase}\left(I_{4a}\right)=0.25\left\{\begin{array}{l}\text{ATAN}\left[\dfrac{I_{4a}-I_{2a}}{I_{1a}-I_{3a}}\right]+\text{ATAN}\left[\dfrac{I_{4a}-I_{2a}}{I_{1b}-I_{3b}}\right]\\ +\text{ATAN}\left[\dfrac{I_{4a}-I_{2c}}{I_{1c}-I_{3a}}\right]+\text{ATAN}\left[\dfrac{I_{4a}-I_{2c}}{I_{1d}-I_{3b}}\right]\end{array}\right\} \quad (1$$

$$\text{Phase}\left(I_{4a}\right)=\text{ATAN}\left\{\frac{I_{4a}-0.5\left(I_{2a}+I_{2c}\right)}{0.25\left(I_{1a}+I_{1b}+I_{1c}+I_{1d}\right)-0.5\left(I_{3a}+I_{3b}\right)}\right\} \quad (2$$

The spatial frequency that the phase can be reconstructed was evaluated by reconstructing a sinusoidal phase profile using the three algorithms above. The sinusoidal phase profile was 1024 by 1024 simulation pixels across. An individual subpixel on the simulated detector was nominally 8 simulation pixels across or 128 by 128 subpixels. The residual variance of each of the three reconstruction algorithms, given a subaperture size of 8 simulation pixels, was compared with the residual error calculated using a test four bin interferometer in which the phase was reconstructed at the macro-pixel level. This test four bin interferometer calculated the phase using four different reference phases at each macro-pixel and incremented the macro-pixel size discreetly in simulation pixels from 2 by 2 to 32 by 32 to determine the relative spatial resolution achievable by the three algorithms given above. The results of these simulations in reconstructing a sinusoidal phase with sixteen subapertures per wavelength is shown in Figure 4, where the solid black line represents the variance of the test interferometer as a function of macro-pixel size ranging from less than one(2 simulation pixels) to four(32 simulation pixels) times the subpixel size(8 simulation pixels) that the three algorithms were reconstructed on. The long dashed gray line represents the variance between the phase

and the average phase over each macro-pixel and it falls on top of the variance of the test interferometer obtained from the simulations. The short dashed gray line represents the analytic variance, $\sigma^2 \sim \zeta^2/12$, as calculated above with the phase step, ζ, equal to the amplitude of the sinusoidal phase divided by the number of macro-pixels in a quarter wavelength. Alg. 1, which reconstructed the phase at the corners of the pixels but only used four adjacent pixels, gave a spatial resolution equivalent to 1.33 subpixels, represented in Fig. 4 as the black triangle. The two algorithms that reconstructed the phase at the centers of the pixels, but required nine adjacent pixels, gave slightly better performance with the reconstruction equivalent to a spatial resolution of 1.15 subpixels using the algorithm of Eq. 1(alg. 2), open black square in Fig. 4, and 1.11 subpixels using Eq. 2(alg. 3), gray circle in Fig. 4. The effective spatial resolution of the three algorithms as a function of the spatial sampling of the sinusoidal phase is shown in Fig. 5. The dashed black line represents alg.1 and varies between an effective spatial resolution of 1.3 subpixels when the phase is well sampled, 128 subapertures per wavelength, to 1.6 subpixels when the phase is sampled with just four subapertures per wavelength. Alg. 3, solid black line, performs slightly better than Alg. 2, solid gray line, ranging from an effective spatial resolution of 1 subpixel with high sampling to 1.7 subpixels when the phase is sampled with just four subapertures per wavelength.

In summary, we have presented and simulated the performance of a novel pixelated spatial phase shifting interferometer using a LC-SLM. This interferometer can be easily reconfigured to provide a range of phase steps. The effective spatial resolution of the four phase level interferometer as a function of sampling for three separate algorithms was investigated. From these results it can be seen that the performance can

be optimized by using the convolution alg., alg. 3, for well sampled wavelengths, $\geq$ 8 subapertures per wavelength, and the nearest neighbor alg., alg. 1, for worse sampling, $\leq$ 4 subapertures per wavelength.

This work was performed under the auspices of the U.S. Department of Energy by the University of California, Lawrence Livermore National Laboratory under contract No. W-7405-Eng-48.

REFERENCES

[1] Katherine Creath, in *Interferogram Analysis: Digital Fringe Pattern Measurement Techniques*, edited by David W Robinson and Graeme T. Reid (Institue of Physics Publishing, Philadelphia, 1993).

[2] James Millerd, John Hayes, Michael North-Morris, Matt Novak and James Wyant, "Pixelated Phase-Mask Dynamic Interferometer," presented at the Interferometry XII: Techniques and Analysis, Denver, CO, 2004.

[3] Carolyn R. Mercer and Katherine Creath, "Liquid-crystal point-diffraction interferometer," Opt. Lett. **19** (12), 916 (1994).

[4] H. Kadono, M. Ogusu, and S. Toyooka, "Phase shifting common path interferometer using a liquid-crystal phase modulator,"Optics Communications **110**, 391 (1994).

[5] Mark J. Guardalben, Lutau Ning, Nieraj Jain, Devon J. Battaglia and Kenneth L. Marshall, "Experimental comparison of a liquid-crystal point-diffraction interferometer (LCPDI) and a commercial phase-shifting interferometer and methods to improve LCPDI accuracy," Appl. Opt **41** (7), 1353 (2002).

[6] Gordon D. Love, Thomas J. D. Oag, and Andrew K. Kirby, "Common path interferometric wavefront sensor for extreme adaptive optics," Optics Express **13** (9), 3491 (2005).

[7] Youichi Bitou, "Digital phase-shifting interferometer with an electrically addressed liquid-crystal spatial light modulator," Opt. Lett. **28** (17), 1576 (2003).

[8] K.L. Baker, E.A. Stappaerts, S.C. Wilks, D. Gavel, P.E. Young, J. Tucker, D.A. Silva, S.S. Olivier and J. Olsen, "Performance of a phase-conjugate-engine implementing a finite-bit phase correction," Opt. Lett. **29** (5), 1576 (2004).

FIGURE CAPTIONS

Figure 1 Twyman-Green(a) and self-referencing point diffraction(b) implementations of the single-shot, pixelated phase-shifting interferometer utilizing a liquid crystal spatial light modulator: BS, beam splitters; PBS, polarizing beam splitter; M, mirrors; L, lenses; F, filter; P, polarizer, respectively.

Figure 2 Applied phase masks for the LC-SLM to obtain three, four and five frame single-shot phase shifting information.

Figure 3 Variance as a function of random phase errors in the phase step arising from miscalibration of or dispersion in, for the case of broadband illumination, the liquid-crystal spatial light modulator.

Figure 4 Effective spatial resolution obtainable with a four-bin macro-pixel reconstructing a sinusoidal phase with sixteen subapertures per wavelength using various reconstruction algorithms.

Figure 5 Examination of the effective spatial resolution of the three algorithms as a function of the spatial sampling of the sinusoidal phase.

FIGURES

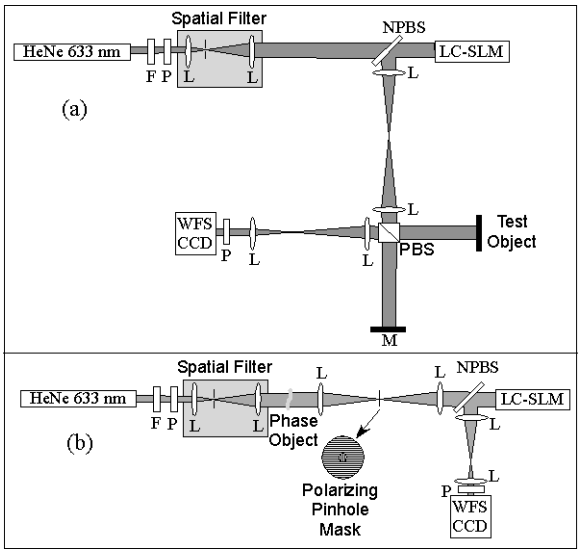

Figure 1

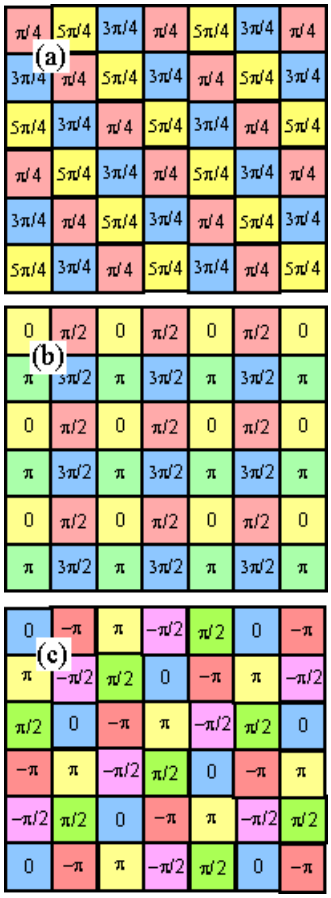
(a)
π/4 5π/4 3π/4 π/4 5π/4 3π/4 π/4
3π/4 π/4 5π/4 3π/4 π/4 5π/4 3π/4
5π/4 3π/4 π/4 5π/4 3π/4 π/4 5π/4
π/4 5π/4 3π/4 π/4 5π/4 3π/4 π/4
3π/4 π/4 5π/4 3π/4 π/4 5π/4 3π/4
5π/4 3π/4 π/4 5π/4 3π/4 π/4 5π/4
(b)
0 π/2 0 π/2 0 π/2 0
π 3π/2 π 3π/2 π 3π/2 π
0 π/2 0 π/2 0 π/2 0
π 3π/2 π 3π/2 π 3π/2 π
0 π/2 0 π/2 0 π/2 0
π 3π/2 π 3π/2 π 3π/2 π
(c)
0 −π π −π/2 π/2 0 −π
π −π/2 π/2 0 −π π −π/2
π/2 0 −π π −π/2 π/2 0
−π π −π/2 π/2 0 −π π
−π/2 π/2 0 −π π −π/2 π/2
0 −π π −π/2 π/2 0 −π

Figure 2

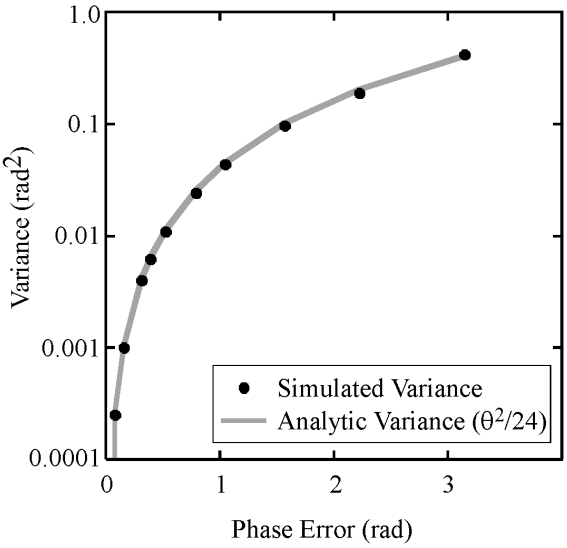
1.0
0.1
0.01
0.001
0.0001
Variance (rad^2)
0
1
2
3
Phase Error (rad)
Simulated Variance
Analytic Variance (θ^2/24)

Figure 3

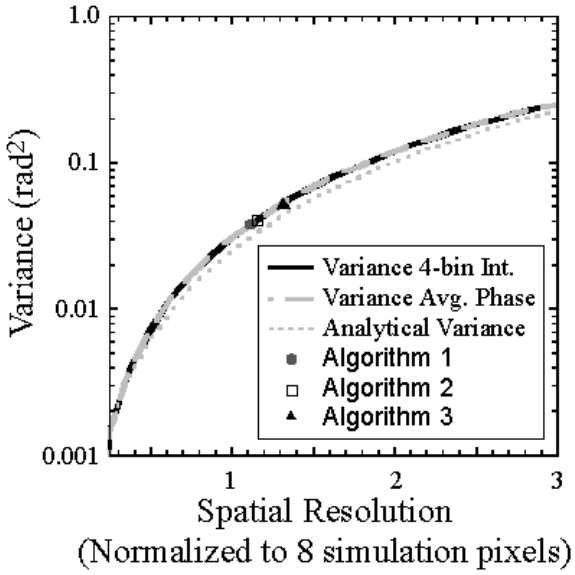
1.0
0.1
0.01
0.001
Variance (rad²)
1
2
3
Spatial Resolution
(Normalized to 8 simulation pixels)
Variance 4-bin Int.
Variance Avg. Phase
Analytical Variance
Algorithm 1
Algorithm 2
Algorithm 3

Figure 4

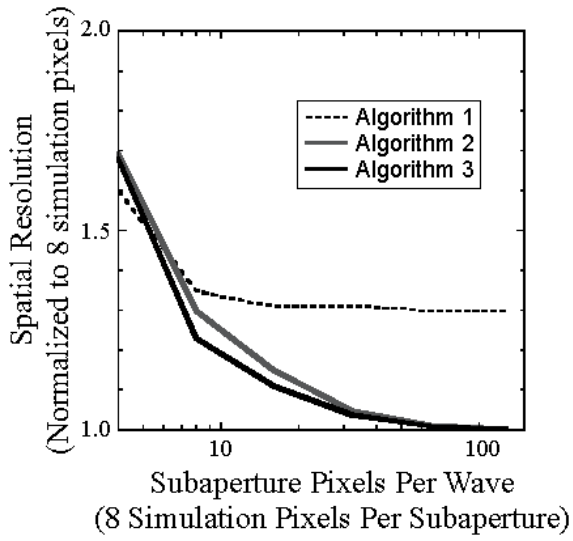
Spatial Resolution
(Normalized to 8 simulation pixels)
2.0
1.5
1.0
10
100
Algorithm 1
Algorithm 2
Algorithm 3
Subaperture Pixels Per Wave
(8 Simulation Pixels Per Subaperture)

Figure 5